Applicability Analysis of Three Atmospheric Radiative Transfer Models in Nighttime

Jiacheng He [1,2], Wenhao Zhang [1,2],*, Sijia Liu [1,2], Lili Zhang [3], Qiyue Liu [1,2], Xingfa Gu [1,3] and Tao Yu [1,3]

[1] School of Remote Sensing and Information Engineering, North China Institute of Aerospace Engineering, Langfang 065000, China; hejiacheng@stumail.nciae.edu.cn (J.H.); liusijia1007@stumail.nciae.edu.cn (S.L.); liuqy_bhht@nciae.edu.cn (Q.L.); guxingfa@radi.ac.cn (X.G.); yutao@radi.ac.cn (T.Y.)

[2] Hebei Collaborative Innovation Center for Aerospace Remote Sensing Information Processing and Application, Langfang 065000, China

[3] Aerospace Information Research Institute, Chinese Academy of Sciences, Beijing 100094, China; zhangll@lreis.ac.cn

* Correspondence: zhangwh@radi.ac.cn

Abstract: The relatively stable lunar illumination may be used to realize radiometric calibration under low light. However, there is still an insufficient understanding of the accuracy of models and the influence of parameters when conducting research on low-light radiometric calibration. Therefore, this study explores the applicability of three atmospheric radiative transfer models under different nighttime conditions. The simulation accuracies of three nighttime atmospheric radiative transfer models (Night-SCIATRAN, Night-MODTRAN, and Night-6SV) were evaluated using the visible-infrared imaging radiometer suite day/night band (VIIRS/DNB) data. The results indicate that Night-MODTRAN has the highest simulation accuracy under DNB. The consistency between simulated top-of-atmosphere (TOA) radiance and DNB radiance is approximately 3.1%, and uncertainty is 2.5%. This study used Night-MODTRAN for parameter sensitivity analysis. The results indicate that for the lunar phase angle, aerosol optical depth, surface reflectance, lunar zenith angle, satellite zenith angle, and relative azimuth angle, the average change rates are 68%, 100%, 2561%, 75%, 20%, and 0%. This paper can help better understand the performance of models under different atmospheric and geographical conditions, as well as whether existing models can simulate the complex processes of atmospheric radiation.

Keywords: radiative transfer model; SCIATRAN; MODTRAN; 6SV; VIIRS/DNB; nighttime

1. Introduction

Radiometric calibration is the premise for the quantitative application of optical satellite data. However, after the payload is launched, it becomes challenging to achieve on-orbit radiometric calibration due to the complexity of the transmission link of the calibration reference on the satellite. Additionally, ground target measurement, which could be used as a reference for site calibration, is often influenced by uncertain factors such as scale effects, atmospheric conditions, and environmental changes [1–4]. At present, the accuracy issue of radiometric calibration for remote-sensing payloads remains an urgent problem that needs to be addressed. Although the application of traditional optical remote-sensing payload radiometric-calibration methods is relatively well-established, research on the radiometric calibration of low-light remote-sensing payloads is still challenging [5–8]. In recent years, there has been the successful launch of more and more satellites equipped with low-light imagers (such as LuoJia1-01, Fengyun-3E, and Sustainable Development Goals Science Satellite-1 (SDGSAT-1)). The application technology of low-light remote sensing has been developed rapidly, which has led to the increasing demand for low-light remote-sensing data. Therefore, it is essential to realize the radiometric calibration of low-light remote-sensing payloads.

Due to the ground light source being relatively stable, it is not influenced by the lunar radiation. Therefore, the active calibration method using ground light has been widely used [9,10]. Cao et al. [11] conducted a study using point sources such as fishing boats, bridges, and urban lights for low-light calibration. The results indicated a good consistent correlation between the estimated light power of bridge lights and the light power retrieved from satellite data. It also suggests designing specially created light sources to minimize uncertainty in low-light calibration. Because the sea surface is a dark background at night, the radiation of cross-sea bridge lights is relatively stable at night. Ma et al. [12] proposed a low-light calibration method based on bridge lights. The Hangzhou Bay Bridge and Donghai Bridge in China were selected as the calibration targets for VIIRS/DNB, with satellite observation data from August 2012 to July 2014 used. A comparison was made between simulated calculated TOA radiance and DNB radiance. The results revealed that the relative error of the low-light calibration method based on the Hangzhou Bay Bridge was $-2.9\% \pm 9.3\%$, and the low-light calibration method based on the Donghai Bridge was $-3.9\% \pm 7.2\%$. Factors such as cloud scattering radiation, traffic signal lights, and vehicle headlamp radiation can easily influence the results during the simulation. Therefore, ground light source-active calibration methods require light sources with long-term stability and direct upward radiation emission capabilities. Hu et al. [13] conducted long-term monitoring of Dunhuang radiation correction field light sources, analyzed DNB imaging rules of target pixels under different observation geometric conditions, and developed a ground light source with stable radiation intensity and uniform directionality in all directions. However, these ground light sources are easily influenced by other light sources, and the type, position, and other factors of ground light sources are difficult to measure directly. Consequently, the on-orbit radiometric calibration of low-light remote-sensing payloads remains a significant challenge in need of resolution.

Recently, a method for the radiometric calibration of low-light remote-sensing payloads has been developed [14–16]. This method entails the selection of multiple low-phase and cloudless low-light remote-sensing images and through long-term sequence observations of uniformly stable targets on the surface. Following radiation transmission simulation calculations, the simulated values are compared with the observed values. Desert areas, due to their relatively stable atmospheric conditions and minimal time-based changes, are frequently utilized as vicarious calibration fields. For instance, Liao et al. [17] selected the Railroad Valley Playa (RVP) Desert in the United States as a vicarious calibration field, choosing 18 near-full-moon RVP observation values from March to October 2012. They used the MODTRAN model combined with the ROLO lunar irradiance model to simulate the TOA radiance at the top of the atmosphere, yielding an average deviation of -6.1% and an uncertainty of 8.9% in radiation error estimation. The albedo of ice and snow is relatively stable in the visible light band, making polar ice and snow coverage areas suitable for vicarious calibration. Qiu et al. [18] selected the Dome C area in Antarctica and the Greenland ice sheet area in the Arctic as vicarious calibration fields. The reflectance at the top of the atmosphere of the calibration area obtained by the lunar irradiance model (MT2009) showed good consistency with the corresponding product of Hyperion, with a radiometric calibration uncertainty of about 8%. Hu et al. [19] compared the difference between simulated TOA and actual observed radiance after a year of observations in the Dome C region of Antarctica and the RVP desert region of the United States. The results indicated average relative errors of -7.14% and -4.14%, respectively. Hu et al. [20] employed a low-light substitution calibration based on the Dunhuang radiation correction field. They analyzed 14 sets of DNB observation data from September 2012 to July 2014. By leveraging Ma et al.'s [21] refined atmospheric radiative transfer models, they obtained simulated TOA radiance values. When compared to actual DNB radiance, the relative error was found to be $-6.2\% \pm 8.6\%$. Given that convective clouds lie above atmospheric aerosols and water vapor, their impact can be disregarded, thereby preventing inaccuracies in atmospheric radiative transfer models. Consequently, Ma et al. [21] introduced a low-light substitution calibration technique based on deep convective clouds. They selected six months of DNB

data spanning August 2012 to January 2013. By integrating the MT2009 lunar irradiance model into the SCIATRAN model, they achieved radiative transfer to compute simulated albedos for target pixels. When comparing these simulated albedos with DNB observations under prevailing observational geometric conditions, the results indicated that the radiative uncertainty stemming from diurnal variations lies within ±10%. In summary, a lot of research has been developed on the radiation calibration of low-light satellites using the nighttime atmospheric radiative transfer model.

While these studies use the nighttime atmospheric radiative transfer model for low-light radiometric calibration, existing models have certain limitations. Firstly, basic research on point source radiation transfer is still underdeveloped in the context of ground light radiometric calibration methods. This lack of maturity hinders the effective application of the radiative transfer model in these studies [22]. Subsequently, in the study of low-light radiometric calibration methods, existing models are susceptible to discrepancies arising from surface properties and weather conditions, leading to significant inaccuracies in their predictions. Therefore, this paper studies the applicability of different atmospheric radiative transfer models at nighttime. This study employs lunar illumination as a radiation source to replace the existing atmospheric radiative transfer models. Then, the nighttime atmospheric radiative transfer model was constructed and compared with the VIIRS/DNB data. Furthermore, the influence of parameters, including lunar phase angle, aerosol optical depth, surface reflectance, lunar zenith angle, observation zenith angle, and relative azimuth angle, on nighttime radiative transfer simulations was meticulously analyzed. This study aims to elucidate the suitability of various radiative transfer models during nighttime, thereby facilitating informed decision making regarding model selection for diverse scenarios. Concurrently, it seeks to advance the development of high-precision nighttime atmospheric radiative transfer models, enhancing the precision of low-light radiometric calibration.

2. Materials and Methods

2.1. Research Region

China National High-Resolution Remote Sensing Integrated Calibration Field, also known as the Baotou Field, is situated in Bayannur City, within China's Inner Mongolia Autonomous Region. Its central coordinates are 40.85° N and 109.62° E, and it is approximately 50 km from the Baotou urban area. The Baotou field has superior basic geographical conditions, flat regional terrain, and uniform surface reflection. The climate in the field is dry, with little rain in four seasons. The annual average rainfall is 320 mm and has good atmospheric visibility conditions [23]. It spans an area of 3.0 km², with a central altitude of 1.27 km [24]. Furthermore, the Baotou Field has an automatic atmospheric parameter observation system, as depicted in Figure 1. This system comprises an automatic sun-tracking photometer, CIMEL CE318, and an automated weather station, which operates in a full-day observation mode to gather atmospheric and meteorological parameters routinely [25]. Consequently, the Baotou Field was selected for the nighttime radiative transfer simulation experiment.
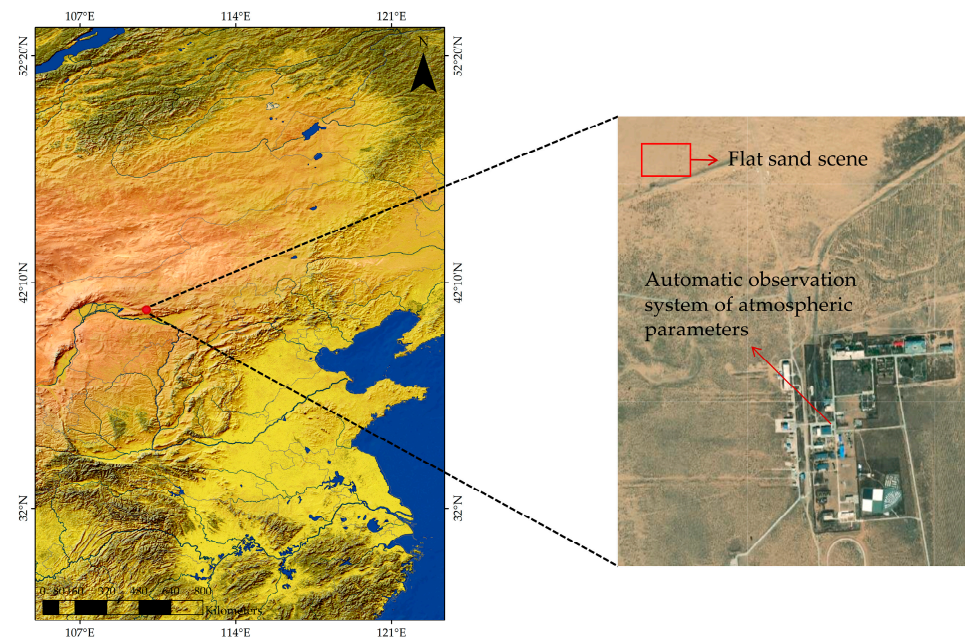
Figure 1. The location of Baotou Field and automatic observation system.

2.2. Data Collection

2.2.1. Nighttime Light Data

The Suomi National Polar-orbiting Partnership (SNPP) is the first satellite of the National Polar-orbiting Environmental Satellite System (NPOESS) in the United States, and VIIRS, as the core payloads of this satellite, is a scanning radiometer with a side-looking scan width of about 3044 km and a revisit cycle of 12 h. There are 22 bands in VIIRS, including 5 high-resolution (I-band), 16 medium-resolution (M-band), and 1 DNB [26,27]. This study used two sets of SNPP data products: SVDNB and GDNBO products composed of 3072×4064 pixels in sensor data records (SDRs). Among them, the SVDNB product provides calibrated TOA radiance, and its quality flags for operational use; the GDNBO product includes latitude and longitude corresponding to the TOA radiance, lunar phase angle, satellite zenith angle, and other observation geometric information [28–30]. The spatial resolution of these data is 750 m, and they are published in HDF5 format. Figure 2 shows the spectral response function of the DNB used. DNB was obtained from https://www.avl.noaa.gov/, accessed on 16 April 2023 [31].

It is essential to filter the VIIRS/DNB data from 2020 to 2022 to ensure accuracy in the final calibration results. The criteria for observation selection are as follows:

(1) The research region is focused on the DNB pixel corresponding to the central location of the Baotou Field, extending outwards to a range of 10 km $\times$ 10 km.

(2) The lunar zenith angle is less than 90°, meaning the moon is positioned above the horizon. This ensures that the lunar illumination can effectively illuminate the target pixel area.

(3) The lunar phase angle is less than 120°, meaning more than two-thirds of the lunar phase is illuminated. This ensures an adequate downward illumination of the top of the atmosphere.
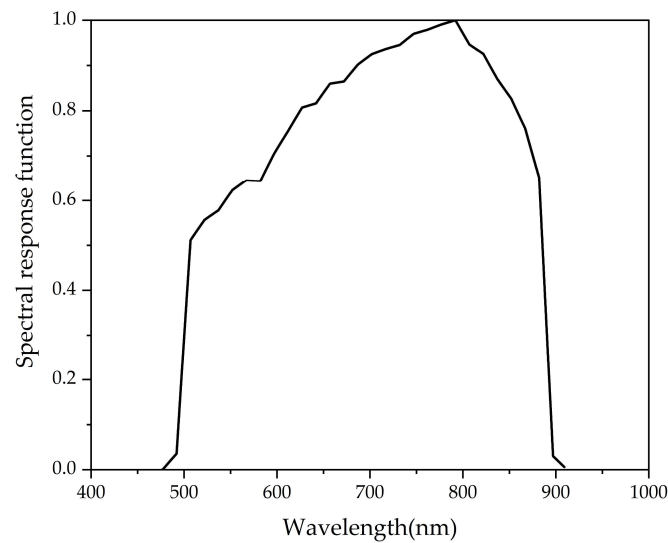
Figure 2. DNB spectral response function.

2.2.2. Surface Reflectance Data

This study utilizes the surface reflectance parameter product, part of the MODIS Level 3 Land Standard Product data. These data represent multi-angle reflectance data derived from the cumulative changes in the solar surface satellite's relative position, as observed over a continuous 16-day period by orbital platforms (TERRA and AQUA). The product is presented as raster data with a spatial resolution of 500 m. In this study, the average surface reflectance of Band1, Band2, and Band4 is used instead of the surface reflectance at DNB.

2.2.3. Aerosol Optical Depth Data

Aerosol Robotic Network (AERONET) is a global aerosol observation network based on ground monitoring, providing long-term aerosol monitoring, and can provide near real-time aerosol information with an observation error of only 0.02. AERONET offers three different quality levels: level 1.0 (uncurated verified), level 1.5 (cloud-curated), and level 2.0 (strict quality assurance) [32]. This study uses the aerosol optical depth (AOD) of level 1.5 at the AOE_BaoTou site. Because the aerosol optical depth at 550 nm is missing in the AERONET measured data, it cannot be used as a parameter input into the atmospheric radiative transfer model [33,34]. Therefore, aerosol optical depth at 550 nm was calculated using Equation (1):

$$\ln \tau_{0.55} = \frac{\ln \tau_{0.675} - \ln \tau_{0.44}}{\ln 0.675 - \ln 0.44} (\ln 0.55 - \ln 0.44) + \ln \tau_{0.44} \tag{1}$$

where $\tau_{0.44}$ and $\tau_{0.675}$ are the aerosol optical depth at wavelengths of 440 nm and 675 nm, and $\tau_{0.55}$ is the aerosol optical depth at 550 nm obtained by interpolation.

2.2.4. Lunar Irradiance Data

The MT2009 is a hyperspectral lunar irradiance model developed by Miller and Turner. It is used to calibrate with VIIRS/DNB data, realizing the quantitative application of nighttime remote-sensing data. The model encompasses a wavelength range from 0.2 μm to 2.8 μm, with a spectral resolution of 1 nm [35]. The irradiance calculated using this model is represented by Equation (2):

$$E_m = L_m \Omega_m = \alpha E_0 \left(\frac{R_{se}}{R_{sm}}\right)^2 \left(\frac{r_m}{R_{me} - r_e}\right)^2 f(\theta_p, \lambda) \tag{2}$$

where L_m is the lunar reflected radiance, Ω_m is the Earth-observed lunar solid angle, R_{se} is the average distance between the sun and Earth, R_{sm} is the average distance between the

sun and moon, r_m is the radius of the moon, r_e is the radius of the Earth, and R_{me} is the average distance between the Earth and moon. While $f(\theta_p, \lambda)$ is the lunar phase function, and its empirical expression is given by Equation (3):

$$f(\theta_p, \lambda) = 10^{-0.4[a(\theta_p) - b(\theta_p)\lambda]} \tag{3}$$

where *a* and *b* are the fitting coefficients of lunar brightness variation with wavelength and phase angle, obtained from the measured data.

The solar irradiance utilized in MT2009 is derived from satellite-based measurement data of Solar Radiation and Climate Experiment (SORCE) [36]. Furthermore, the model fits the geometric relationship of sun–moon–Earth. It also provides the lunar phase angle, the mean distance between the sun and the moon, and the average distance between Earth and the moon at varying times. Figure 3 illustrates the lunar irradiance under different lunar phase angles, considering the average distance between the sun and the moon and the average distance between Earth and the moon.
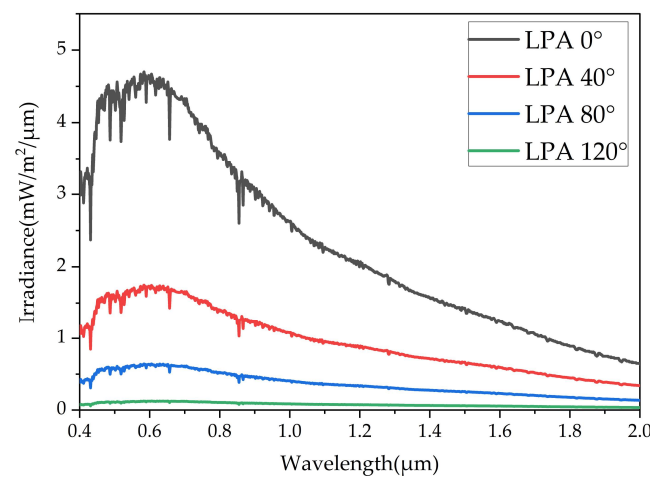

Figure 3. Lunar irradiance simulated by MT2009 under different lunar phase angles.

This section presents the data used in this paper and the data processing. Table 1 describes the details of the datasets used in this paper.

Table 1. Statistics of datasets.

Data	Product/Model	Spatial/Spectrum Resolution	Date/Waveband
Nighttime Light Data	SVDNB, GDNBO	750 m	April 2020 to November 2022
Surface Reflectance Data	MCD43A4(C6)	500 m	April 2020 to November 2022
Aerosol Optical Depth Data	AOE_BaoTou site	ground station	April 2020 to November 2022
Lunar Irradiance Data	MT2009	1 nm	400 nm to 2000 nm

2.3. Methods

Figure 4 shows the workflow of this study. It involves data collection and processing, model construction, model precision evaluation, and model sensitivity analysis.

(1) Data collection and processing: This study used SNPP satellite data, surface reflectance data, aerosol optical depth data, lunar irradiance data, and DNB spectral response function. The SNPP satellite data were processed by Geographic Lookup Table (GLT) correction. The surface reflectance data are reprojected to the WGS84 coordinate system. The aerosol optical depth at 550 nm was obtained by interpolating aerosol data. The resolution of lunar irradiance data is converted into three formats: 1 nm, 0.5 nm, and 1 cm^{-1}.

(2) Model construction: This study analyzes the characteristics of lunar radiation for the MT2009 lunar irradiance model. The lunar irradiance is introduced into MODTRAN, SCIATRAN, and 6SV, and the lunar illumination is used as the radiation source of the atmospheric radiative transfer model.

(3) Model precision evaluation: The radiance value of the SVDNB product was used as a benchmark to evaluate the accuracy of simulated values from three nighttime atmospheric radiation transfer models. Then, the accuracy of the nighttime atmospheric radiative transfer model is evaluated by calculating the average relative error.

(4) Model sensitivity analysis: Utilizing the nighttime atmospheric radiative transfer model, calculated the sensitivity of different parameters to the TOA radiance, including lunar phases, aerosol optical depths, surface reflectances, lunar zenith angles, and observation zenith angles. Concurrently, the applicability of the atmospheric radiative transfer model under different conditions is further analyzed.
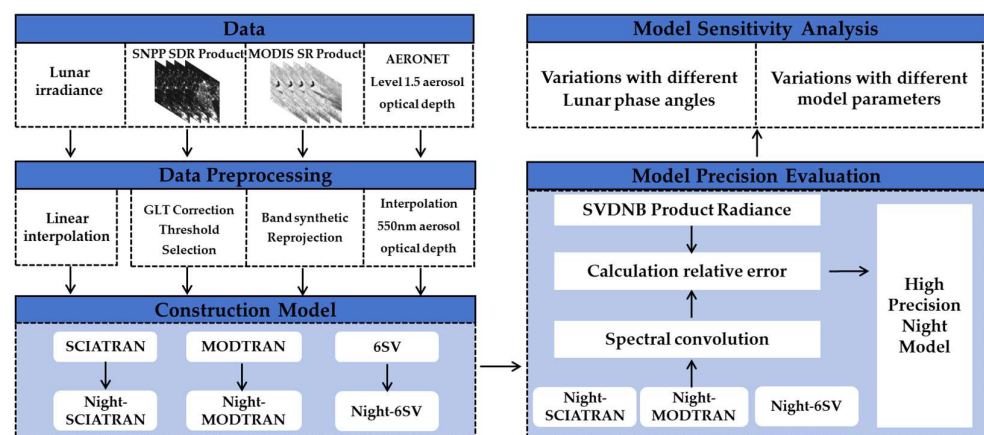

Figure 4. Flow chart of this study.

2.3.1. Principle of Atmospheric Radiative Transfer at Nighttime

Figure 5 is the path diagram of atmospheric radiative transfer at nighttime. As shown in Figure 5, the TOA lunar radiation undergoes atmospheric extinction before reaching the surface; after ground reflection, its radiance, along with that emitted by ground artificial lights and other sources, undergoes atmospheric effects and is received and recorded by satellite sensors [7,9]. At present, it is difficult to quantify the radiation of ground lights accurately, and related research on the ground light model is still underway. Therefore, to ensure the calculation's accuracy, this paper chooses the area without ground lights. This area is located in the calibration site of Baotou, China, which is far from the city center, so ground lights will not affect it.

When the impact of atmospheric absorption is not taken into account, the downward irradiance $E_{\downarrow Lunar}$ of lunar illumination after atmospheric attenuation can be expressed as Equation (4):

$$E_{\downarrow Lunar} = \mu_L E_L D_\downarrow(\theta_L) \tag{4}$$

where μ_L is the cosine of the lunar zenith angle, E_L is the TOA lunar irradiance, $D_\downarrow(\theta_L)$ is the downward transmission rate, and θ_L is the lunar zenith angle.

When lunar radiation reaches the surface, it undergoes reflection by the ground and absorption. The lunar radiation reflected by the ground will reach the atmosphere after being continuously scattered between the atmospheric boundary and the surface. Equations (5) and (6) are used to calculate this reflected lunar irradiance.

$$E = E_{\downarrow Lunar}[ar + a^2r^2 + L]r$$
$$= \mu_L E_L D_\downarrow(\theta_L)\frac{r}{1-ar} \tag{5}$$

$$L = \frac{E}{\pi} = \mu_L E_L D_\downarrow(\theta_L)\frac{r}{1-ar} \tag{6}$$

where a is the albedo of the atmospheric hemisphere, r is the ground reflectance, and L is the lunar irradiance the ground reflects.

When the lunar radiation reaches the surface, it will be reflected and absorbed by the ground. Lunar radiation reflected by the ground will eventually reach the atmosphere after continuous scattering between the atmospheric boundary and the surface. The radiance received by the sensor is expressed in Equation (7):

$$L_{TOA} = \frac{D_\uparrow(\theta_V)r\mu_L E_L D_\downarrow(\theta_L)}{\pi(1-ar)} + L_{path} \tag{7}$$

where L_{TOA} is the TOA radiance, $D_\uparrow(\theta_V)$ is the atmospheric uplink transmittance, θ_v is the satellite zenith angle, and L_{path} is the path radiance.
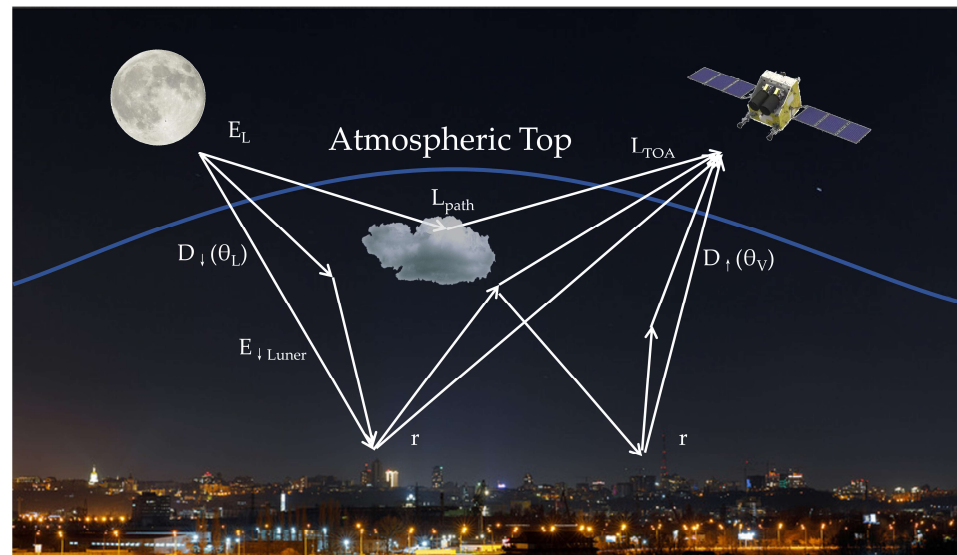

Figure 5. Nighttime atmospheric radiation transmission process.

2.3.2. Construction Process of Nighttime Atmospheric Radiative Transfer Models

This study used three atmospheric radiative transfer models: SCIATRAN, MODTRAN, and 6SV. Because 6SV model was used to simulate high spectral TOA reflectance over the entire visible and near-infrared spectral range. This facilitated the calibration of satellite's low radiance using 6SV model [37]. The high-resolution model, SCIATRAN, has been used in low-light radiometric calibration studies at Dome C in Antarctica, the Railroad Valley Playa (RVP) desert region in the USA, and the Dunhuang radiometric correction field [19,20,38]. Meanwhile, the mid-resolution model, MODTRAN, operating in lunar mode, has been used to assess the accuracy of the in-orbit radiometric calibration of low-light satellites and to simulate lunar radiation transmission [39].

SCIATRAN is a high spectral-resolution model with a spectral range of 175–2400 nm and a spectral resolution of 0.24–0.5 nm. The SCIATRAN software package used in this study is version 4.6. MODTRAN is an enhanced version of LOWTRAN, covering the spectral range of 0–22,600 cm^{-1}. It has a spectral resolution of 2 cm^{-1}, making it a medium-resolution atmospheric radiation transfer model. The MODTRAN software package used in this study is version 5. 6SV is a vector model developed based on the 6S model. Researchers have considered the polarization characteristics of the atmosphere and surface and further

enriched parameters such as scattering angle, wavelength node, aerosol vertical profile, etc. The 6SV software package used in this study is version 2.1. Then, the MT2009 was combined with SCIATRAN, MODTRAN, and 6SV, and these three modified atmospheric radiation transfer models will be employed to simulate the nighttime radiation transfer process.

Firstly, the solar spectrum files within the three atmospheric radiative transfer models must be substituted with lunar irradiance files from the MT2009 model. However, due to a discrepancy between the spectral resolution of the atmospheric radiative transfer model and that of the lunar irradiance file, it is necessary to obtain three distinct resolutions of lunar irradiance via interpolation processing to accommodate different atmospheric radiative transfer models. In this study, SCIATRAN has a spectral resolution of 0.5 nm, MODTRAN has a spectral resolution of 1 cm^{-1}, and 6SV has a spectral resolution of 1 nm.

Secondly, it is also necessary to interpolate the DNB spectral response function files to facilitate the convolution of simulated TOA radiance with spectral response functions. This ensures a consistent resolution.

Ultimately, the simulated TOA radiance at different wavelengths must be convolved with that wavelength's corresponding spectral response function. This process will yield the simulated TOA radiance at the DNB, as depicted in Equation (8):

$$P = \frac{\int_{\lambda_{s(i)}}^{\lambda_{e(i)}} P(\lambda) S_i(\lambda) d\lambda}{\int_{\lambda_{s(i)}}^{\lambda_{e(i)}} S_i(\lambda) d\lambda} \tag{8}$$

where P is the simulation TOA radiance, $P(\lambda)$ is the simulated radiance under different wavelengths, i is the band, $\lambda_{s(i)}$ and $\lambda_{e(i)}$ are the start and end wavelengths of the range of this band, and $S_i(\lambda)$ is the spectral response function of the corresponding band.

2.3.3. Parameter Settings of Nighttime Atmospheric Radiative Transfer Models

When using Night-SCIATRAN to simulate the TOA radiance, it is necessary to set the type of calculation results, radiation transmission mode, and other parameters in the model (Table 2).

Table 2. The Night-SCIATRAN parameter setting.

Parameter Name	Assignments	Description
RTM_MODE	int	Radiance
RTM_TYPE	spher_scat	Spherical Atmospheric Scattering Model
RTM_CORE	DOM	Discrete ordinate method
Extra-terrestrial solar flux	File	Extracting spectral data from designated files
Spectral segment info	1 492.5, 833, 0.5	Choice of Expression and Band Range
Forward model: trace gases	all	Consider all trace gases
Line absorber treatment	esft	Linear Absorbing Gas
Aerosol settings	advanced	User-defined aerosol parameters (as controlled by the control_aer.inp file)
Latitude & Longitude	40.85, 109.62	Longitude and Latitude of research region

When using Night-MODTRAN to simulate the TOA radiance, it is necessary to set the atmospheric model, geometric conditions, and other parameters in the model (Table 3).

When using Night-6SV to simulate the TOA radiance, it is necessary to set the aerosol type, spectral conditions, and other parameters in the model (Table 4).

Table 3. The Night-MODTRAN parameter setting.

Module	Parameter Name	Assignments
Module 1	Model Atmosphere	MidLatitude Summer
	Type of Atmospheric Path	Slant Path to Space or Ground
	Mode of Execution	Radiance with Scattering
	Execute with Multiple Scattering	MS on Flux at Observer
	Scattering Algorithm	DISORT algorithm
	Surface Reflectance	0~1
	Solar Database Option	User-supplied file
Module 2	Aerosol Model Used	Rural–VIS = 23 km
	Seasonal Modifications to Aerosols	Spring-Summer
	Surface Meteorological/Visible Range	0~1
	Zenith Angle (deg)	0~180
	Radius of Earth (km)	6371
Module 3	Initial Frequency (nm)	500
	Final Frequency (nm)	900
	Day of Year	1~365
	Azimuth Angle of Observer LOS (deg)	−180~180
	Lunar Zenith Angle (deg)	0~90

Table 4. The Night-6SV parameter setting.

Line Number	Input Parameter	Description
1	0	User selects geometric conditions
2	40 50 20 30 7 7	Input geometric condition parameters: solar zenith angle, solar azimuth angle, satellite zenith angle, satellite azimuth angle, month and day.
3	2	Mid-latitude summer atmospheric patterns
4	5	Aerosol model is desert-type
5	0	The chosen method for aerosol content input is 550 nm optical depth
6	0~1	Aerosol Optical Depth
7	−1.27	The target altitude is 1.27 km
8	−1000	Sensors on Satellites
9	100	Spectral conditions for the VIIRS/DNB channel (user-defined)
10	0	Uniform surface
11	0	Unidirectional reflection characteristics
12	0~1	Surface reflectance
13	−2	No Activation of Atmospheric Correction Method

3. Results

3.1. Models Precision Evaluation

SVDNB products of the Baotou Field were collected from April to November each year between 2020 and 2022. Finally, 30 sets of nighttime data that fit the observation conditions were obtained (Table A1). Figure 6 shows the variation in simulated TOA and DNB radiance with observation time for different models. The average relative error and uncertainty of the observed data are calculated to quantitatively describe the relative error between the difference between DNB radiance and simulated TOA radiance. As can be seen from Figure 6, the average relative error and uncertainty of Night-SCIATRAN are −14.8% ± 8.2%, Night-6SV are 66.6% ± 8.8%, and Night-MODTRAN are 3.1% ± 2.5% (Table 5). Therefore, the Night-MODTRAN has the best accuracy among the three models in this experiment. The sources of errors and uncertainties in the results may be mainly caused by surface reflectance, aerosols, lunar zenith angle, etc.
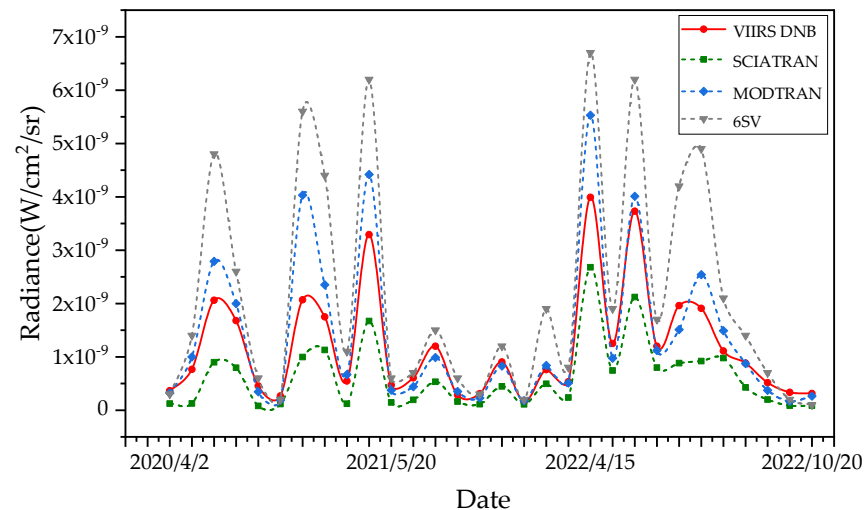
Figure 6. Simulation results of TOA radiance and their comparison.

Table 5. Accuracy evaluation of three nighttime radiative transfer models.

Model	Average Relative Error	Uncertainty
Night-SCIATRAN	−14.8%	8.2%
Night-6SV	66.6%	8.8%
Night-MODTRAN	3.1%	2.5%

It is noted that the characteristics of the atmosphere and surface can introduce errors and uncertainties into the model. First of all, in the radiative transfer model, it is typically assumed that the surface exhibits homogeneous characteristics. However, upon closer examination, it becomes evident that the surface possesses distinct directional reflection properties [40]. Moreover, the data on surface reflectance show that it is coarse (spatial resolution of 500 m). This limitation is a detailed description of alterations in surface reflectance characteristics, particularly in regions by cities or vegetation-covered surfaces. Another possible source of error and uncertainties can be the inaccurate characterization of aerosol optical depth. Due to the current uneven distribution of AERONET sites, it is impossible to monitor on a large scale. And the diurnal variation in aerosols is large, and there will still be biased situations using aerosol daily average data [41]. Consequently, the overestimation of aerosol optical depth could cause the overestimation of simulated results and vice versa.

In addition, it can also be seen from Figure 6 that the TOA radiance simulated by Night-MODTRAN is closest to the DNB observation value, followed by the TOA radiance simulated by Night-SCIATRAN, while the difference between the TOA radiance simulated by Night-6SV and the DNB observation is the largest. Therefore, the results of this experiment show that the simulation results of Night-MODTRAN have the best accuracy and are suitable for nighttime radiative transfer simulations. Night-6SV has the worst accuracy and should be used carefully for nighttime radiative transfer simulations.

Correspondingly, after comparing the nighttime radiative transfer model of other scholars with the model of this study, it was found that the performance of Night-MODTRAN is better than that of other models (Table 6).

In this study, in order to further analyze the variability characteristics of the nighttime radiative transfer simulation, the error analysis of Night-MODTRAN is carried out by using the relative error (*RE*) and absolute error (*AE*), as shown in Equations (9) and (10).

$$RE = \frac{L_{exp} - L_{obs}}{L_{obs}} \times 100\% \qquad (9)$$

$$AE = \left| L_{exp} - L_{obs} \right| \qquad (10)$$

Table 6. Statistics based on accuracy evaluation of nighttime radiative transfer model.

Atmospheric Radiative Transfer Model	Lunar Irradiance Model	Evaluation Accuracy	Reference
MODTRAN	ROLO	$-6.1\% \pm 8.9\%$	Liao et al. [17]
SCIATRAN	MT2009	$-6.2\% \pm 8.6\%$	Hu et al. [20]
MODTRAN	MT2009	$3.1\% \pm 2.5\%$	This study

Figure 7 shows the relative error distribution with respect to the lunar phase angle, and it can be seen that the relative error is relatively scattered in the longitudinal, basically varying within the range of −35% to 40%, which is within an acceptable error range [20,42]. The calculation results show that when the lunar phase angle is smaller, the simulated TOA radiance is usually greater than the DNB radiance. When the lunar phase angle is larger, the simulated TOA radiance is generally less than the DNB radiance.
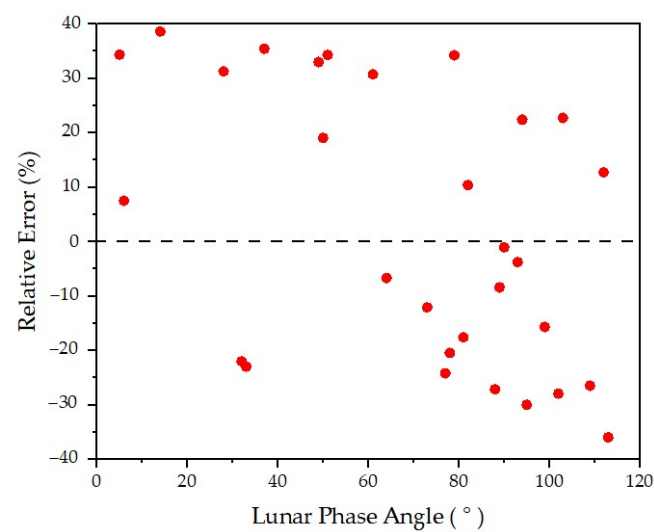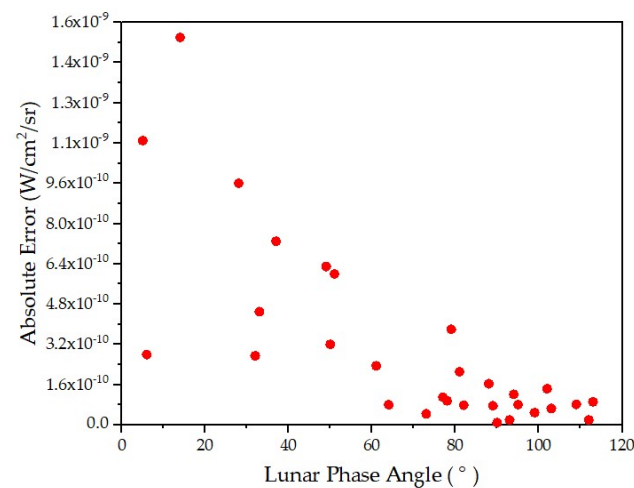

Figure 7. The distribution of relative error with the lunar phase angle.

Figure 8 shows the distribution of absolute errors with the lunar phase angle. It can be seen that as the lunar phase angle increases, the absolute error between the simulated TOA radiance and the DNB radiance gradually decreases, and the absolute error value tends to be stable at the lunar phase angle of $90°$. The results show that the absolute error can be ensured in the appropriate range when the lunar phase angle is near $90°$.

Figure 8. The distribution of absolute error with the lunar phase angle.

3.2. Sensitivity Analysis

This section develops the sensitivity analysis of the parameters such as lunar phase angles, aerosol optical depths, surface reflectances, lunar zenith angles, satellite zenith angles, and relative azimuth angles. The sensitivity parameters are changed in a certain range while keeping the other parameters in Night-MODTRAN unchanged. Table 7 lists the sensitivity parameters' specific reference value and input range.

Table 7. Parameter settings.

Input Parameter	Reference Value	Input Range	Parameter Setting
Lunar phase angle	0°	0°~120°	Interval 40° (4 groups)
Aerosol optical depth	0.1	0~1	Interval 0.1 (11 groups)
Surface reflectance	0.1	0~1	Interval 0.1 (11 groups)
Lunar zenith angle	0°	0°~80°	Interval 10° (9 groups)
Satellite zenith angle	180°	110°~180°	Interval 10° (8 groups)
Relative azimuth angle	0°	−180°~180°	Interval 40° (13 groups)

Figure 9 illustrates the change trends of simulated TOA radiance with five parameters under four lunar phase angles. As can be seen from Figure 9, the simulated TOA radiance increases with the increase in aerosol optical depth and surface reflectance, and the average change rates are 100% and 2561%. The simulated TOA radiance decreases with the increase in the lunar phase angle, lunar zenith angle, and satellite zenith angle, and the average change rates are 68%, 75%, and 20%. However, there was no significant change with the increase in the relative azimuth angle.
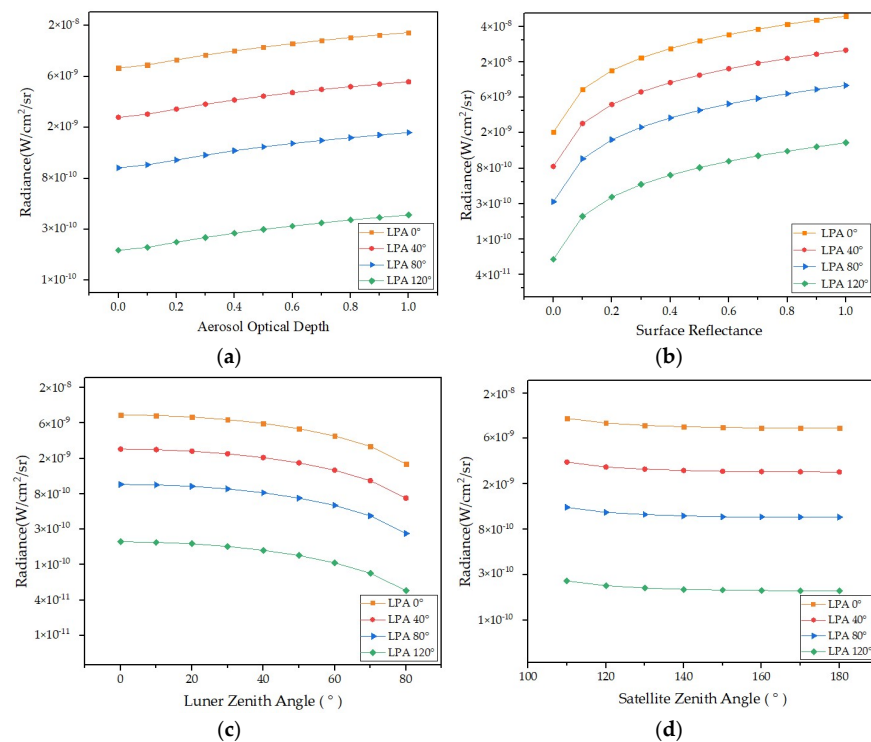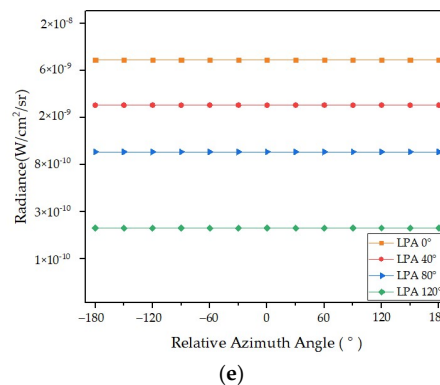

Figure 9. *Cont.*

(**e**)

Figure 9. The simulated TOA radiance change trends with different parameters under four lunar phase angles: (**a**) aerosol optical depth, (**b**) surface reflectance, (**c**) lunar zenith angle, (**d**) satellite zenith angle, and (**e**) relative azimuth angle.

When the average change rate is greater than 50%, the parameter is considered to be sensitive to the simulated TOA radiance [17,43]. Therefore, the results show that the simulated TOA radiance is sensitive to the changes in lunar phase angle, aerosol optical depth, surface reflectance, and lunar zenith angle. The simulated TOA radiance is not sensitive to the changes in the satellite zenith angle and relative azimuth angle.

4. Discussion

This study explores the applicability of atmospheric radiative transfer models under different nighttime conditions from two aspects: the model's accuracy and the parameters' sensitivity. Utilizing the VIIRS/DNB observation data as a radiation benchmark, the simulation accuracy of three nighttime atmospheric radiation transfer models was analyzed. The results indicate that Night-MODTRAN offers superior accuracy, with a relative error range of 3.1% $\pm$ 2.5%. This is followed by Night-SCIATRAN, which presents a relative error range of $-14.8\% \pm 8.2\%$, and Night-6SV, which demonstrates the poorest accuracy with a relative error range of 66.6% $\pm$ 8.8%. An assessment of the relative error between simulated TOA radiance and DNB radiance indicates that this error ranges from -35% to 40%, and the simulated TOA radiance fluctuates greatly. The absolute error is larger when the lunar phase angle is less than 90°, with smaller lunar phase angles correlating to larger errors. However, the error fluctuation is not obvious when the lunar phase angle falls between 90° and 120°. It is advisable to select conditions with a smaller lunar phase angle and stronger lunar radiation when the error gap is not apparent, as this can avoid some image noise. Consequently, this study suggests that the radiative transfer simulation calculation methods for lunar phase angles proximate to 90° are most suitable for low-light remote-sensing payloads radiometric calibration.

The sensitivity of Night-MODTRAN was examined with respect to parameters such as lunar phase angle, aerosol optical depth, surface reflectance, lunar zenith angle, satellite zenith angle, and relative azimuth angle. The findings indicate that the TOA radiance is most sensitive to surface reflectance variations; the average change rate is 2561%. This can be attributed to the higher surface reflectance value resulting in a brighter surrounding environment, leading to increased reflected radiation received by the satellite sensor. Therefore, high-precision surface reflectance data must be provided when simulating the TOA radiance. However, the TOA radiance shows no sensitivity to the relative azimuth angle, and the average change rate is 0%. It may be that the TOA radiance is less influenced by the relative azimuth angle during the simulation process, ensuring a consistent size of lunar radiation [44,45].

Due to the influence of solar stray light on the lunar illumination and the impact of clouds on atmospheric radiation, the construction of nighttime atmospheric radiation transfer models will produce errors. Consequently, the DNB nighttime observation data of clear sky and cloudless in Baotou Field are obtained using visual identification methods. For

satellite sensors with low spatial resolutions, such as AVHRR and MODIS, an approximate 10 km × 10 km area near the center of the research region is typically utilized as a substitute for the target site for calibration. Considering the spatial resolution of DNB to be 750 m, which is deemed low. This study selected satellite observation data from a 10 km × 10 km area near the center of the Baotou Field for analysis and processing.

The successful application of low-light detection data, from the inception of the Defense Meteorological Satellite Program–Operational Linescan System (DMSP/OLS) to VIIRS/DNB, is largely contingent upon the precise radiometric calibration of payload detection data [46]. Through the results of this study, a highly accurate nighttime radiative transfer model can be obtained, thereby achieving accurate radiometric calibration. And research studies have shown that an accurate nighttime radiative transfer model also plays an important role in the field of nighttime atmospheric parameter inversion [47]. It is noted that the VIIRS/DNB measurements of nighttime emission are mainly from the moon and ground lights. In future works, the contribution of ground lights should be quantified, and an atmospheric radiative transfer model for point sources on the ground should be established. This will be of great significance to improve the accuracy of the nighttime radiative transfer model.

5. Conclusions

This study constructs nighttime atmospheric radiative transfer models by integrating the MT2009 lunar irradiance model into the atmospheric radiative transfer model. The current state of different atmospheric radiative transfer models in nighttime simulations is analyzed using the VIIRS/DNB nighttime observation data. After experimental verification, three conclusions have been drawn.

(1) In this study, the relative error range for Night-SCIATRAN is $-14.8\% \pm 8.2\%$, that for Night-6SV is $66.6\% \pm 8.8\%$, and for Night-MODTRAN is $3.1\% \pm 2.5\%$. The results indicate that the simulation accuracy of Night-MODTRAN is optimal for nighttime radiative transfer simulations.

(2) By calculating the relative error between simulated and DNB radiance, it has been found that when the lunar phase angle is smaller, the simulated TOA radiance is usually higher than the DNB radiance. Conversely, when the lunar phase angle is larger, the simulated TOA radiance is usually lower than the DNB radiance. The absolute error fluctuation tends to be stable near the lunar phase angle of $90°$.

(3) In this study, the simulated TOA radiance is sensitive to the changes in the lunar phase angle, aerosol optical depth, surface reflectance, and lunar zenith angle, and the average change rates are 68%, 100%, 2561%, and 75%. However, the simulated TOA radiance is not sensitive to the changes in satellite zenith angle and relative azimuth angle, and the average change rates are 20% and 0%.

In summary, the nighttime radiative transfer model is significant for the radiometric calibration of low-light satellite remote sensing. This study analyzed the applicability of three atmospheric radiative transfer models under different nighttime conditions. It provides an important reference for future research on the radiometric calibration methods of low-light remote-sensing payloads, as well as for understanding the radiative processes of the nighttime atmospheric system. Currently, the atmospheric radiative transfer model effectively captures the impact of the atmosphere on parallel light radiation transfer. Nonetheless, a substantial gap persists in fundamental theoretical research concerning radiation transfer from point sources within the atmosphere. Future research should focus on point light source radiative transfer models and the incorporation of ground lights into nighttime radiative transfer models. These will broaden the model's application range and enhance its accuracy.

Appendix A

Table A1 shows that 30 sets of nighttime satellite data from 2020 and 2022 were used for the model's precision evaluation in Section 3.1.

Table A1. The 30 sets of nighttime satellite data used for the model's precision evaluation.

NO.	Lunar Phase Angle	Aerosol Optical Depth	Surface Reflectance	Lunar Zenith Angle	Lunar Azimuth Angle	Satellite Zenith Angle	Satellite Azimuth Angle
1	73°	0.189	0.195	84.78°	−65.63°	26.02°	−74.81°
2	61°	0.187	0.196	73.31°	−78.72°	2.54°	90.39°
3	37°	0.142	0.200	60.93°	161.26°	44.44°	96.39°
4	50°	0.189	0.201	70.58°	144.89°	59.19°	92.94°
5	78°	0.263	0.207	83.31°	−73.27°	37.93°	97.44°
6	95°	0.164	0.205	85.29°	102.16°	44.75°	96.35°
7	28°	0.075	0.196	51.59°	−174.26°	16.98°	−75.78°
8	50°	0.134	0.187	49.12°	137.58°	38.05°	97.35°
9	94°	0.162	0.197	56.23°	88.11°	2.67°	100.84°
10	5°	0.094	0.200	61.82°	−137.38°	7.53°	−78.86°
11	78°	0.342	0.208	83.11°	−77.43°	38.21°	96.79°
12	89°	0.116	0.198	72.43°	107.84°	21.68°	99.26°
13	81°	0.135	0.187	66.80°	100.68°	62.72°	92.20°
14	103°	0.139	0.187	64.94°	89.14°	8.11°	−78.68°
15	109°	0.182	0.163	71.89°	73.12°	29.79°	97.78°
16	89°	0.219	0.170	63.09°	81.66°	54.49°	93.91°
17	112°	0.194	0.172	74.14°	82.80°	26.86°	−75.05°
18	82°	0.112	0.182	60.94°	101.24°	18.47°	−76.62°
19	93°	0.169	0.181	65.86°	94.06°	11.06°	100.64°
20	14°	0.195	0.214	54.80°	−132.70°	21.90°	98.90°
21	32°	0.106	0.215	80.50°	−104.20°	62.90°	−68.20°
22	6°	0.105	0.214	70.40°	−138.10°	33.30°	−74.90°
23	64°	0.232	0.217	72.70°	148.70°	40.10°	−73.40°
24	33°	0.166	0.216	66.90°	178.30°	33.30°	−74.40°
25	49°	0.054	0.179	43.16°	149.85°	2.02°	99.35°
26	78°	0.390	0.178	41.41°	99.49°	1.77°	89.59°
27	89°	0.208	0.180	52.99°	85.64°	29.78°	98.53°
28	102°	0.145	0.200	64.45°	80.66°	1.94°	111.13°
29	113°	0.218	0.201	78.36°	74.03°	40.73°	98.59°
30	99°	0.467	0.188	79.35°	98.95°	7.07°	−78.97°

References

1. Lyapustin, A.; Wang, Y.; Choi, M.; Xiong, X.; Angal, A.; Wu, A.; Doelling, D.R.; Bhatt, R.; Go, S.; Korkin, S.; et al. Calibration of the SNPP and NOAA 20 VIIRS sensors for continuity of the MODIS climate data records. *Remote Sens. Environ.* **2023**, *295*, 113717. [CrossRef]
2. Cui, Z.; Ma, C.; Zhang, H.; Hu, Y.; Yan, L.; Dou, C.; Li, X.M. Vicarious Radiometric Calibration of the Multispectral Imager Onboard SDGSAT-1 over the Dunhuang Calibration Site, China. *Remote Sens.* **2023**, *15*, 2578. [CrossRef]
3. Zhang, Q.; Zhao, Y.; Zhang, L.; Wu, J.; Li, W.; Yan, J.; Jiang, X.; Yan, Z.; Zhao, J. On-Orbit Radiometric Calibration of Hyperspectral Sensors on Board Micro-Nano Satellite Constellation Based on RadCalNet Data. *Remote Sens.* **2022**, *14*, 4720. [CrossRef]
4. Chen, Y.; Sun, K.; Li, W.; Hu, X.; Li, P.; Bai, T. Vicarious Calibration of FengYun-3D MERSI-II at Railroad Valley Playa Site: A Case for Sensors with Large View Angles. *Remote Sens.* **2021**, *13*, 1347. [CrossRef]
5. Che, H.; Zhang, X.; Chen, H.; Damiri, B.; Goloub, P.; Li, Z.; Zhang, X.; Wei, Y.; Zhou, H.; Dong, F. Instrument calibration and aerosol optical depth validation of the China Aerosol Remote Sensing Network. *J. Geophys. Res. Atmos.* **2009**, *114*, D03206. [CrossRef]
6. Hu, X.; Liu, J.; Sun, L.; Rong, Z.; Li, Y.; Zhang, Y.; Zheng, Z.; Wu, R.; Zhang, L.; Gu, X. Characterization of CRCS Dunhuang test site and vicarious calibration utilization for Fengyun (FY) series sensors. *Can. J. Remote Sens.* **2014**, *36*, 566–582. [CrossRef]
7. Min, M.; Deng, J.; Liu, C.; Guo, J.; Lu, N.; Hu, X.; Chen, L.; Zhang, P.; Lu, Q.; Wang, L. An investigation of the implications of lunar illumination spectral changes for Day/Night Band-based cloud property retrieval due to lunar phase transition. *J. Geophys. Res. Atmos.* **2017**, *122*, 9233–9244. [CrossRef]
8. Qiu, S.; Shao, X.; Cao, C.Y.; Uprety, S.; Wang, W.H. Assessment of straylight correction performance for the VIIRS Day/Night Band using Dome-C and Greenland under lunar illumination. *Int. J. Remote Sens.* **2017**, *38*, 5880–5898. [CrossRef]
9. Xi, S.; Changyong, C.; Sirish, U. Vicarious calibration of S-NPP/VIIRS day-night band. *Proc. SPIE* **2013**, *8866*, 88661S. [CrossRef]
10. Zakharov, Y.N.; Popov, A.Y.; Tyurin, A.V. Semiconductor laser's on-line coherence calibration and testing of frequency stability. *Proc. SPIE* **2008**, *7008*, 70081P. [CrossRef]
11. Cao, C.; Bai, Y. Quantitative Analysis of VIIRS DNB Nightlight Point Source for Light Power Estimation and Stability Monitoring. *Remote Sens.* **2014**, *6*, 11915–11935. [CrossRef]
12. Ma, S.; Yan, W.; Huang, Y.; Jiang, J.; Hu, S.; Wang, Y. Calibration Method of Low-Light Sensor Based on Bridge Lights. *J. Atmos. Ocean. Technol.* **2016**, *33*, 1123–1134. [CrossRef]
13. Hu, S.; Ma, S.; Yan, W.; Lu, W.; Zhao, X. Feasibility of a specialized ground light source for night-time low-light calibration. *Int. J. Remote Sens.* **2018**, *39*, 2543–2559. [CrossRef]
14. Yang, H.; Zhou, J.; Weng, F.; Sun, N.; Anderson, K.; Liu, Q.; Kim, E.J. Developing Vicarious Calibration for Microwave Sounding Instruments Using Lunar Radiation. *IEEE T. Geosci. Remote* **2018**, *56*, 6723–6733. [CrossRef]
15. Ryan, R.E.; Pagnutti, M.; Burch, K.; Leigh, L.; Ruggles, T.A.; Cao, C.; Aaron, D.; Blonski, S.; Helder, D.L. The Terra Vega Active Light Source: A First Step in a New Approach to Perform Nighttime Absolute Radiometric Calibrations and Early Results Calibrating the VIIRS DNB. *Remote Sens.* **2019**, *11*, 710. [CrossRef]
16. Elvidge, C.D.; Baugh, K.E.; Zhizhin, M.; Hsu, F.-C. Why VIIRS data are superior to DMSP for mapping nighttime lights. *Proc. Asia-Pac. Adv. Netw.* **2013**, *35*, 62. [CrossRef]
17. Liao, L.B.; Weiss, S.; Mills, S.; Hauss, B. Suomi NPP VIIRS day-night band on-orbit performance. *J. Geophys. Res. Atmos.* **2013**, *118*, 12705–12718. [CrossRef]
18. Qiu, S.; Shao, X.; Cao, C.; Uprety, S. Feasibility demonstration for calibrating Suomi-National Polar-Orbiting Partnership Visible Infrared Imaging Radiometer Suite day/night band using Dome C and Greenland under moon light. *J. Appl. Remote Sens.* **2016**, *10*, 16024. [CrossRef]
19. Hu, S.; Ma, S.; Yan, W.; Huang, Y. Using two different targets for the calibration of S-NPP VIIRS day night band under lunar illumination. *Proc. SPIE* **2016**, *10255*, 102552O. [CrossRef]
20. Hu, S. VIIRS Low-Light Channel Data Radiometric Calibration and Application Technology. Ph.D. Dissertation, National University of Defense Technology, Wuhan, China, 2019; pp. 27–38.
21. Ma, S.; Yan, W.; Huang, Y.-X.; Ai, W.-H.; Zhao, X. Vicarious calibration of S-NPP/VIIRS day–night band using deep convective clouds. *Remote Sens. Environ.* **2015**, *158*, 42–55. [CrossRef]
22. Li, X.; Elvidge, C.; Zhou, Y.; Cao, C.; Warner, T. Remote sensing of night-time light. *Int. J. Remote Sens.* **2017**, *38*, 5855–5859. [CrossRef]
23. Li, Y.; Chen, M.; Liu, J.; Zhang, Z.; Gao, W. Enhancing research and application of urban rainwater harvesting and utilisation. *Inn. Mong. Water Resour.* **2007**, *4*, 120–121.
24. Tang, H.; Xiao, C.; Shang, K.; Wu, T.; Li, Q. Radiometric Calibration of GF5-02 Advanced Hyperspectral Imager Based on RadCalNet Baotou Site. *Remote Sens.* **2023**, *15*, 2233. [CrossRef]
25. Barreto, Á.; Cuevas, E.; Granados-Muñoz, M.-J.; Alados-Arboledas, L.; Romero, P.M.; Gröbner, J.; Kouremeti, N.; Almansa, A.F.; Stone, T.; Toledano, C.; et al. The new sun-sky-lunar Cimel CE318-T multiband photometer—A comprehensive performance evaluation. *Atmos. Meas. Tech.* **2016**, *9*, 631–654. [CrossRef]
26. Hlaing, S.; Harmel, T.; Gilerson, A.; Foster, R.; Weidemann, A.; Arnone, R.; Wang, M.; Ahmed, S. Evaluation of the VIIRS ocean color monitoring performance in coastal regions. *Remote Sens. Environ.* **2013**, *139*, 398–414. [CrossRef]

27. Wolfe, R.E.; Lin, G.; Nishihama, M.; Tewari, K.P.; Tilton, J.C.; Isaacman, A.R. Suomi NPP VIIRS prelaunch and on-orbit geometric calibration and characterization. *J. Geophys. Res. Atmos.* **2013**, *118*, 11508–11521. [CrossRef]

28. Hu, S.; Ma, S.; Yan, W.; Jiang, J.; Huang, Y. A new multichannel threshold algorithm based on radiative transfer characteristics for detecting fog/low stratus using night-time NPP/VIIRS data. *Int. J. Remote Sens.* **2016**, *38*, 5919–5933. [CrossRef]

29. Ma, Y.; Zhang, W.; Zhang, L.; Gu, X.; Yu, T. Estimation of Ground-Level PM$_{2.5}$ Concentration at Night in Beijing-Tianjin-Hebei Region with NPP/VIIRS Day/Night Band. *Remote Sens.* **2023**, *15*, 825. [CrossRef]

30. Ma, Y.; Zhang, W.; Chen, X.; Zhang, L.; Liu, Q. High Spatial Resolution Nighttime PM$_{2.5}$ Datasets in the Beijing–Tianjin–Hebei Region from 2015 to 2021 Using VIIRS/DNB and Deep Learning Model. *Remote Sens.* **2023**, *15*, 4271. [CrossRef]

31. Chen, H.; Xiong, X.; Sun, C.; Chen, X.; Chiang, K. Suomi-NPP VIIRS day-night band on-orbit calibration and performance. *J. Appl. Remote Sens.* **2017**, *11*, 036019. [CrossRef]

32. He, Q.; Zhang, M.; Huang, B.; Tong, X. MODIS 3 km and 10 km aerosol optical depth for China: Evaluation and comparison. *Atmos. Environ.* **2017**, *153*, 150–162. [CrossRef]

33. Zhang, W.; Xu, H.; Zheng, F. Aerosol Optical Depth Retrieval over East Asia Using Himawari-8/AHI Data. *Remote Sens.* **2018**, *10*, 137. [CrossRef]

34. Zhang, W.; Xu, H.; Zhang, L. Assessment of Himawari-8 AHI Aerosol Optical Depth over Land. *Remote Sens.* **2019**, *11*, 1108. [CrossRef]

35. Zeng, X.; Li, C. The Influence of Heterogeneity on Lunar Irradiance Based on Multiscale Analysis. *Remote Sens.* **2019**, *11*, 2696. [CrossRef]

36. Mauceri, S.; Pilewskie, P.; Woods, T.; Béland, S.; Richard, E. Intercomparing Solar Spectral Irradiance from SORCE SIM. *Earth Space Sci.* **2020**, *7*, e2019EA001002. [CrossRef]

37. Bassani, C.; Sterckx, S. Calibration of Satellite Low Radiance by AERONET-OC Products and 6SV Model. *Remote Sens.* **2021**, *13*, 781. [CrossRef]

38. Mei, L.; Rozanov, V.; Rozanov, A.; Burrows, J.P. SCIATRAN software package (V4.6): Update and further development of aerosol, clouds, surface reflectance databases and models. *Geosci. Model Dev.* **2023**, *16*, 1511–1536. [CrossRef]

39. Yakunin, M.A.; Yurchenko, A.V. MODTRAN5 simulations of responses from MODIS spectroradiometer channels. *Tech. Phys.* **2015**, *60*, 141–144. [CrossRef]

40. Wang, J.; Zhou, M.; Xu, X.; Roudini, S.; Sander, S.P.; Pongetti, T.J.; Miller, S.D.; Reid, J.S.; Hyer, E.; Spurr, R. Development of a nighttime shortwave radiative transfer model for remote sensing of nocturnal aerosols and fires from VIIRS. *Remote Sens. Environ.* **2020**, *241*, 111727. [CrossRef]

41. Okpalaonwuka, C.; Olusegun, C.F.; Olusola, A.; Ogunjo, S. Validation of MODIS AOD retrievals in West Africa: A comparison with AERONET observations. *Air Qual. Atmos. Health* **2023**, *16*, 2085–2094. [CrossRef]

42. Li, J.; Qiu, S.; Zhang, Y.; Gao, C.; Qian, Y.; Liu, Y. Performance assessments of VIIRS DNB on-orbit radiometric calibration accuracy and stability on SNPP and NOAA-20. *J. Infrared Millim. Waves* **2021**, *40*, 809–819. [CrossRef]

43. Min, M.; Zheng, J.; Zhang, P.; Hu, X.; Chen, L.; Li, X.; Huang, Y.; Zhu, L. A low-light radiative transfer model for satellite observations of moonlight and earth surface light at night. *J. Quant. Spectrosc. Radiat. Transf.* **2020**, *247*, 106954. [CrossRef]

44. Feng, Q.; Yang, P.; Kattawar, G.W.; Hsu, C.N.; Tsay, S.-C.; Laszlo, I. Effects of particle nonsphericity and radiation polarization on retrieving dust properties from MODIS observations. *J. Aerosol. Sci.* **2009**, *40*, 776–789. [CrossRef]

45. Stathopoulou, M.; Cartalis, C. Downscaling AVHRR land surface temperatures for improved surface urban heat island intensity estimation. *Remote Sens. Environ.* **2009**, *113*, 2592–2605. [CrossRef]

46. Zhao, Y.; Qu, Z.; Zhang, Y.; Ao, Y.; Han, L.; Kang, S.; Sun, Y. Effects of human activity intensity on habitat quality based on nighttime light remote sensing: A case study of Northern Shaanxi, China. *Sci. Total. Environ.* **2022**, *851 Pt 1*, 158037. [CrossRef]

47. Deng, J.; Qiu, S.; Zhang, Y.; Cui, H.; Li, K.; Cheng, H.; Liu, Z.; Dou, X.; Qian, Y. Estimating Nighttime PM$_{2.5}$ Concentration in Beijing Based on NPP/VIIRS Day/Night Band. *Remote Sens.* **2023**, *15*, 349. [CrossRef]